# Towards experiments using quantum detector tomography to determine the limits of human vision

van Steenis, Natan

# Towards experiments using quantum detector tomography to determine the limits of human vision

THESIS

submitted in partial fulfillment of the
requirements for the degree of

BACHELOR OF SCIENCE
in
PHYSICS


| | |
|---|---|
| Author : | Natan van Steenis |
| Student ID : | s2548739 |
| Supervisor : | Dr. Wolfgang Löffler |
| Second supervisor: | Dr. Tom van der Reep |
| Second corrector : | Prof. dr. Jan van Ruitenbeek |


Leiden, The Netherlands, July 24, 2023

# Towards experiments using quantum detector tomography to determine the limits of human vision

**Natan van Steenis**

Huygens-Kamerlingh Onnes Laboratory, Leiden University
P.O. Box 9500, 2300 RA Leiden, The Netherlands

July 24, 2023

## Abstract

Over the past century, scientists have tried to find the minimum number of photons that is required to evoke a visual response of humans. Using single-photon sources, researchers found that humans most likely can indeed detect single photons with an above-chance probability. In this project, an experimental setup is developed towards firstly using quantum detector tomography to determine the accuracy of the human eye to observe few-photon number states. The setup contains two optical beams, one to fixate the eye of the subject and one to target the photons at the proper area of the retina. The focus position and beam divergence are determined with three different methods. Additionally, simulations of the eye show that reliable experiments on humans can be conducted using the devised setup. First tests with humans show that the setup fulfils the requirements and we can reliably target the desired spots on the retina. It is further shown that both the head and the orientation of the eye are stable enough to perform reliable experiments using human observation.

# Contents

Version of July 24, 2023– Created July 24, 2023 - 13:47

Chapter 1

# Introduction

Since it was established that light can be seen as a stream of photons, researchers have tried to determine the minimal number of photons necessary to create visual perception. Hecht et al. [1] showed that five to seven photons are enough to produce visual perception. The development of single-photon sources allowed to directly look at the response to a single photon. Using a heralded single photon source in a 2-alternative forced-choice (2AFC) method Tinsley et al. found an average correct response of $0.516 \pm 0.010$ [2]. In the 2AFC method, the single photon was presented to the subject in one of two intervals, and the subject had to choose in which interval the photon was presented. From this experiment, Tinsley et al. concluded that humans have an above-chance probability to detect single photons. This evidence is promising but the statistics are not very strong. In this research project a novel technique, which was never used before to study human perception is used to study the limit of human visual perception.

## 1.1 Quantum detector tomography on human eyes

This novel technique is based on the work of Reep et al. [3]. They have made a theoretical model, showing that quantum detector tomography can be used to determine the sensitivity of human vision in the few-photon regime. In quantum detector tomography, the characteristics of a detector can be determined by measuring its response to light pulses with known photon number statistics [4]. In this experiment, coherent light pulses with Poisson photon statistics are used and the detector that is characterised is

the human eye.
In the final experiment, test subjects will be placed in a dark room. The experimental procedure will be similar to the experiment conducted by Tinsley et al. In one of two intervals, a pulse from a few-photon Poissonian source will be targeted on a specific area of the retina. Subjects will have to choose in which interval the pulse was presented. The experiment will be repeated for different mean photon numbers of the source. By fitting a model to the experimentally obtained data, the accuracy of the human eye to perceive n photons can be determined. The fact that higher-photon number accuracies can be determined is a big advantage of this method over experiments done with single photon sources.

Moreover, it has been shown that this model works when accounting for factors such as attention span, which is an important limiting factor for experiments with human subjects. The goal of this project is to work towards the experimental realisation of this model. Possible equipment necessary for the experiment was tested, and the experimental setup was built. The current setup consists of a headlock and two arms. The headlock keeps the head stable. One arm is used to send a fixation beam, and the other arm is to send the few-photon light pulses onto the area of the retina with the highest rod density. The equipment was tested using both CCD detection and human subjects. These tests are crucial to determine if the equipment used in the current setup is feasible to perform the final experiment.

There are two main reasons why research into the absolute limit of human vision is highly relevant. Firstly, research on the visual limit will give valuable insights into the way the eye and human perception work. These insights will be very useful to study all signal transfers occurring in the nervous system. Single photons produce extremely small signals, this opens up new pathways to examine noise during signal transfer, which is present in all stages of the signal transduction. The second important reason is that this research combines quantum mechanics with human perception. Combining the two could lay the basis for experimental testing of the fundamentals of quantum theory, done with direct human observation. This could give insights into the gap between the world we normally observe, and the fascinating phenomena like quantum superposition and nonlocality that arise from quantum theories. An area under special scientific interest is the usage of human vision as observers to test entanglement [5].

In Chapter 2 we will describe the biological processes involving photon absorption and signal transfer in the eye. Different noise factors that are potentially limiting reliable single photon perception are also discussed. In Chapter 3 we will show the techniques necessary to implement detector tomography in real experiments. In Chapter 4 the current setup and the methods to analyze the found beam data are discussed. The measured beams are then shown and analyzed in Chapter 5. In Chapter 6 we discuss the first tests done with human observation.

Chapter 2

# The human visual system

Light that enters the eye is focused by the lens onto the retina. The retina is a membrane that consists of millions of rod and cone cells. Rod cells are the most sensitive type of cell to low light levels so this cell will be the focus of this chapter. The incoming photons are first absorbed in the rod cells. From the rods, the signal first goes through rod bipolar cells, after which the signal goes through amacrine cells, cone bipolar cells and finally to ganglion cells [6, 7]. This process, in which each cell communicates to the next cell that a photon is absorbed is from here on referred to as 'the signal'. This is of course a simplified view since for each cell there are multiple different subtypes and each cell receives and sends signals from and to multiple cells [8, 9]. From the ganglion cells, the signal is transferred to the brain. In this chapter, we explore the process of photon absorption in the rod cell and the consequent signal transfer through different cells towards the brain.

## 2.1 Rod density and the optic disc

The density of rods differs between different areas of the retina. The density of rods in the retina is displayed in Fig. 2.1.

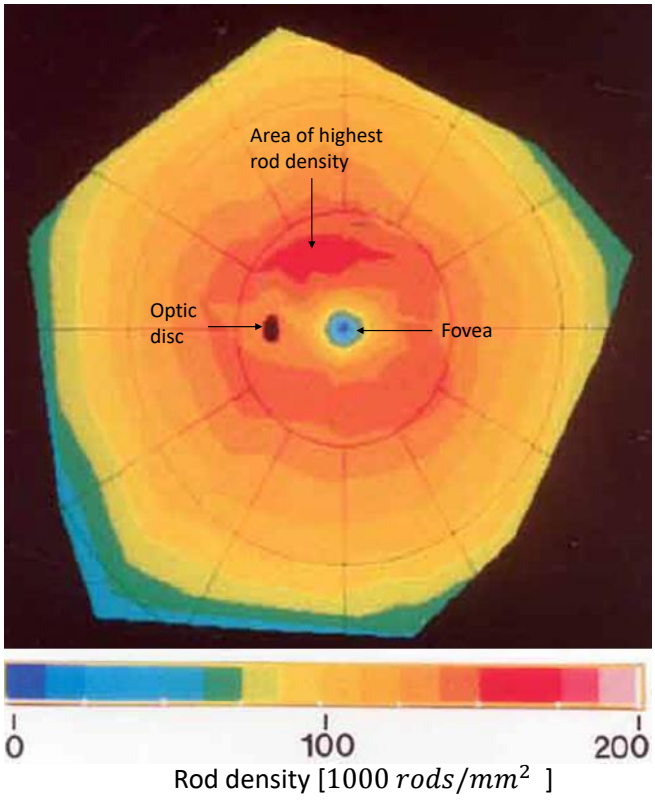


***Figure 2.1:*** *The densities of rods in the human eye. The figure is in the polar azimuthal equidistant projection, meaning that distances are preserved along the meridians, adapted from [10]. The optic disc lies towards the nose as seen from the fovea, referenced to as the nasal side in literature.*

Note that the horizontal distance between the fovea and the optic disc is approximately the same as the vertical distance between the fovea and the highest rod density. This is very useful since it can easily be confirmed if the optic disc is targeted. Under the assumption that the eye is rotationally symmetric, one could change the vertical angle to target the area with the highest rod density. The horizontal angular distance between the fovea and the centre of the optic disc is $0.27 \pm 0.02$ rad and their vertical angular distance is $-0.026 \pm 0.016$ rad [11]. Directions on the retina are defined as nasal and temporal, where nasal means 'towards the nose'. The next important dimension is the size of the optic disc. The mean vertical angular optic disc diameter is 0.075 rad and the mean horizontal optic disc diameter is 0.071 rad [12]. Angular diameters in this thesis will refer to the visual angle, which is a quantity to state the size of an image on the retina

[13]. For the calculations in this thesis, the distance between the lens and the retina is taken to be 20 mm [14].

## 2.2 Photon absorption in the rod cell

The general structure of the rod cell and the connection with the rod bipolar cell in darkness is depicted in Fig. 2.2.

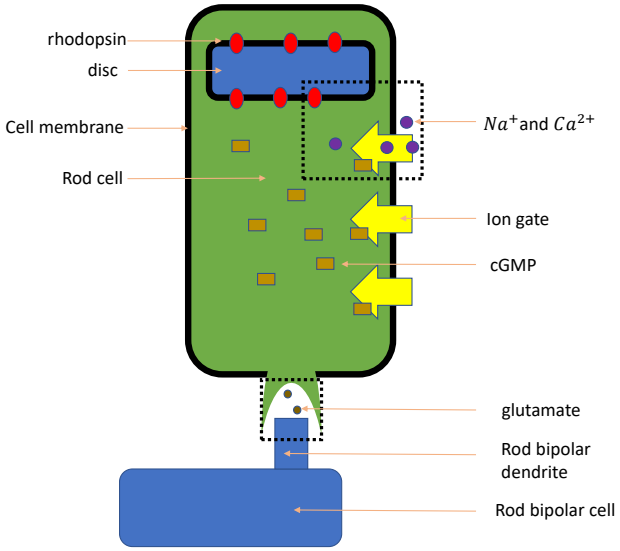


***Figure 2.2:*** *A schematic view of the rod cell and the rod bipolar cell in darkness. The two sections within the dashed squares will be explored in more detail in Fig. 2.3. In reality, the rod cell contains around 1000 discs.*

In darkness, a steady current of $Na^+$ and $Ca^{2+}$ flows through the gates in the rod membrane, creating a voltage of 40 mV over the membrane of the rod cell [15]. The opening and closure of these channels is dependent on a specific nucleotide, called cGMP. The gates are open when a cGMP is bound to them. A rod cell contains around 1000 disks, which contain rhodopsin proteins on its membrane.

The specific processes that are followed by photon absorption are shown in Fig. 2.3. Upon absorbing a photon, the rhodopsin is converted to an active state denoted RH*. RH* then activates the protein transducin. A single rhodopsin can activate around 5 to 10 transducin proteins [16].

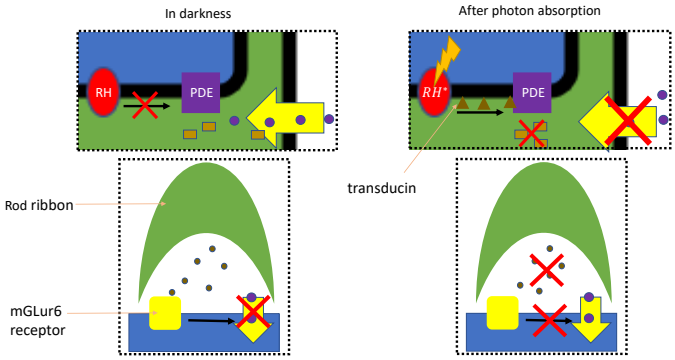


***Figure 2.3:*** *Zoom in of the dotted section of Fig. 2.2. The upper two pictures depict the processes in the rod cell. The lower two pictures depict processes between the rod cell and the rod bipolar cell.*

Each transducin then activates a single enzyme called Phosphodiesterase (PDE), which starts breaking down the cGMP nucleotides. A single photon absorption leads to the breakdown of around $10^5$ cGMP molecules [17], which will result in a reduction of the cGMP concentration in the cell. An important property of cGMP molecules for single photon detection is that the cGMP molecules can spread between the different discs. Without this property, cGMP molecules would quickly deplete around the PDE enzyme. This would not create a strong enough signal. Because of the diffusion of the cGMP molecules, PDE can destroy much more cGMP molecules, which results in a larger number of ion gates being closed. The incoming current of ions will decrease, leading to a small hyperpolarization of the rod cell. Around 5% of the channels are closed after a single photon absorption [detection of single photons by toad and mouse rods], which results in a 1-2 pA reduction to the inward current [18].

## 2.3 Rod to rod bipolar cell signalling

Around 20 rods are connected to a single rod bipolar cell [19]. The transfer of the signal of the photon absorption happens between a specialised ribbon of the rod cell and the dendrite of the rod bipolar cell. In darkness, a specialised ribbon of the rod cell continuously releases the neurotransmitter glutamate [17]. The glutamate receptors mGluR6 on the bipolar cell dendrite sense the glutamate. When mGLuR6 detects glutamate, it acti-

vates a cascade that results in the closure of ion gates on the rod bipolar cell. The increase of the potential over the membrane of the rod cell (hyperpolarization) causes a reduction of the glutamate release. Because of this mGLuR6 will not be activated anymore, resulting in the opening of the ion channels. This results in the depolarization of the bipolar cell. This depolarization will then signal the absorption of a photon to the amacrine cell.

## 2.4 Interneural pathway of rod signalling

From the rod bipolar cell, the signal follows a complicated route to the brain. Their exact pathway is a topic of active research and goes beyond the scope of this thesis. More important is the general mechanism through which signals caused by few-photon absorption are transferred between cells. From the rod bipolar cell, the signal goes to the amacrine cells, and from there it has two possible pathways to the brain[20]. The two different pathways are shown in Fig. 2.4. A signal can either go through Off cone bipolar cells and Off ganglion cells, called the Off pathway. From the amacrine cells, the signal can also go through On cone bipolar cells and On parasol cells, called the On pathway.

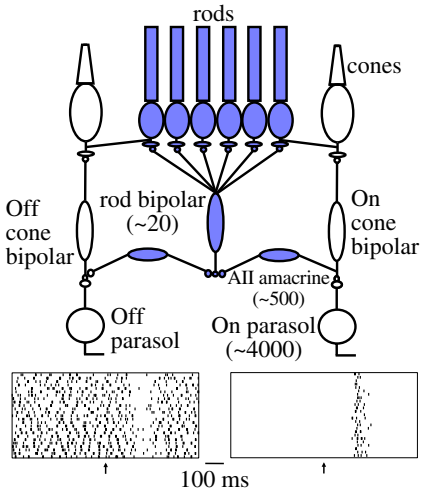


***Figure 2.4:*** *Figures show the differences between On and Off pathways. The black points indicate the firing rate of neurotransmitters and the black arrow indicates an incoming signal. The x-axis of the plot is in time. The numbers next to the different cells indicate the number of rod cells the specific cell got input from. Parasol cells are a specific type of ganglion cell. Adapted from [20].*



Version of July 24, 2023– Created July 24, 2023 - 13:47

The difference between the two pathways is how a signal is communicated from one cell to the next. In darkness, cells in the Off pathway continuously emit transmitters, which are then detected by receptors on the next cell. When a light signal transfers through the cells the transmitter emission is stopped, communicating to the next cell there is a light signal. The On pathway functions in reverse. In darkness, the cells emit no transmitters and a light signal is communicated to the next cell by emitting transmitters. These different mechanisms produce different sensitivities and false positives. Signals at the limits of human vision have a lower chance of being processed through the On pathway. However, the On pathway also has a much lower false positive rate in this regime [21]. The exact mechanism will be explored further in the next section.

## 2.5 Noise in the visual system

Since we are looking at the absolute threshold of vision, the intrinsic noise factors in the eye become very significant. The noise in the rod cell can be divided into two types: shot noise and continuous noise [22]. Both of these will have to be accounted for in the final experiment.

### 2.5.1 Shot noise

Shot noise originates from the spontaneous thermal activation of rhodopsin [23]. The amplitude and time course of this noise is the same as for a real photon absorption thus the two are indistinguishable. The number of spontaneous rhodopsin activation per rod cell per second was measured to be $0.0063 \pm 0.0018 RH^*/\text{rod}/\text{s}$ in monkey cells [24]. More recent research found a value around $0.0034 \pm 0.0008 RH^*/\text{rod}/\text{s}$ [25]. Both experiments were done on isolated dark adapted rod cells. Mamallian rod cells contain around $10^8$ rhodopsin molecules [15]. Assume a spontaneous activation of $0.0034 RH^*/\text{rod}/\text{s}$, this gives a spontaneous activation of a single rhodopsin molecule of around once every 1000 years, which is extremely impressive. So what effect will these spontaneous activations have on the experiment? In this experiment, the angular area that was targeted by the beam had a diameter of 0.017 rad. This converts to a diameter of 0.34 mm, which gives an area $S$ on the retina of $\pi \cdot 0.17^2 = 0.091$ mm$^2$. Assuming we target the area where the rod density is $160 \cdot 10^3$ rods/mm$^2$ the number of spontaneous activations in this region is:

$$0.091\text{mm}^2 \cdot 160 \cdot 10^3 \text{rods}/\text{mm}^2 \cdot 0.0034 RH^*/\text{rod}/s = 49 RH^*/\text{s} \quad (2.1)$$



Version of July 24, 2023– Created July 24, 2023 - 13:47

This means that we would have to filter out the single photon absorption from the 50 photon signals created by noise, which would make single photon experiments almost impossible. Such a high signal to noise ratio would also raise questions about the minimal necessary numbers of photons needed for a visual response determined in previous research. This problem is still unresolved, but one should remember that these noise values were determined in separated pieces of primate retina tissue. The noise in humans might be lower and the effects of keeping the retina tissue in a laboratory environment are also unknown.

### 2.5.2 Continuous noise

The PDE complex destroys cGMP molecules when it is activated by transducin. However, PDE can also activate spontaneously. This spontaneous activation is important to maintain a steady cGMP concentration in darkness [26]. This spontaneous activation fluctuates, which causes a constant fluctuation in the current over the rod membrane [23]. The standard deviation of this noise was measured in monkey rods. It was mesaured to to be either 20 to 25% [25] or $19 \pm 5\%$ of the peak amplitude of a single photon response [27].
A signal-to-noise ratio (SNR) of around 5 might seem quite good. However, when many rods converge to a single rod bipolar cell the signal from the single rhodopsin activation will be swamped. This is caused by the fact that the standard deviation of the integrated noise is proportional to the square root of the number of independent noise sources [27]. If 25 rod signals would be summed up linearly at the rod bipolar cell, the single photon signal would be completely masked. This would make reliable single photon detection impossible.
However, research has found that the signal transfer from the rod to the rod bipolar cell does not happen linearly, but nonlinearly [28]. Only rod signals above a certain threshold value will be processed by the rod bipolar cell, see Fig 2.5.



Version of July 24, 2023– Created July 24, 2023 - 13:47

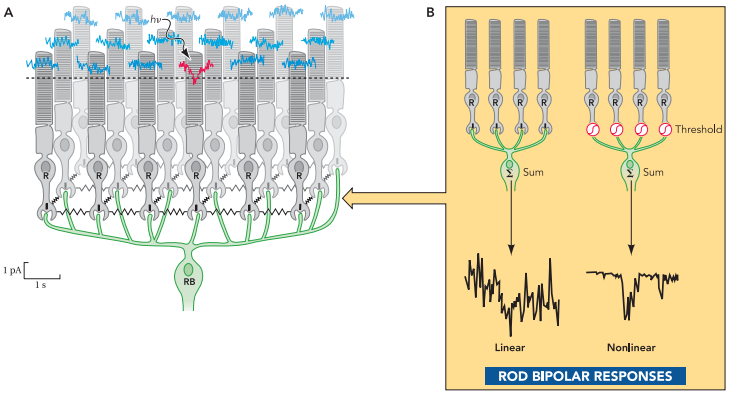


***Figure 2.5:*** *(a) The convergence of many rod cells (R) to a single rod bipolar cell (RB). The blue lines indicate continuous electrical noise and the red line indicates a real photon absorption. (b) The difference in the observed signal of the rod bipolar cell when the input from the rod cells is processed linearly and non-linearly. Adapted from [17]*

.

The exact processes that cause the thresholding and the exact position of the threshold are still a topic of ongoing research. In mice, the threshold seems to be around 1.3 times the average single photon response [28]. At this threshold, around 75 % of the single photon responses are eliminated. However, the benefit is that this increases the SNR by around 350-fold.
Signal thresholding is not exclusive to the rod to rod-bipolar connection, but is also seen between other cells involving the signal transfer. In section 2.4 the different false positive rates and probability that a single photon signal is processed between the On and the Off pathway were discussed. This difference between the On and Off pathway also lies in the fact that signal processing in the On pathway happens nonlinear, whereas signals in the Off pathway are processed mostly linear [20]. This explains the far lower false positive rate in the On pathway.

Chapter 3

# Quantum detector tomography for testing single photon human vision

In the previous chapter, we have given an overview of the important biophysical aspects of the eye. In this chapter, we discuss the details of the experimental procedure. In the first section, we explain the photon statistics of Poissonian light and motivate why Poissonian light is used. After this, the theoretical method to determine the n-photon state detection accuracy of the eye will be shortly discussed. In the last two sections, we discuss the principles to direct the photons to the correct area of the retina.

## 3.1 Poissonian light

As mentioned in the introduction, we use a coherent light source with a Poissonian number distribution. Since there are single photon sources researched and available within our group [29, 30], and single photon sources have been employed in human vision experiments [2, 31], one might ask why those sources were not used to conduct this experiment. There are several reasons for this. First, with quantum detector tomography not only the sensitivity to single-photon detection but also to n-photon number states in general can be determined. Second, a reliable single photon source is hard to make and is currently not available in our group in the green wavelength range, where the rod cells are most sensitive.
In the quantum mechanical view, light is no longer described as a wave but as a stream of light quanta named photons [32]. To explore the proper-

ties of light, we can imagine an experiment where such a photon stream is examined with a single photon detector. The beam is characterised by taking small time bins and determining the number of photons per time bin. When these bins are made small enough, the average number of photons per bin becomes fractional. But photons are described by discrete packages so the number of photons must be an integer. This will cause fluctuations in the photon number on small time scales, even when the average photon flux is constant. This experiment is schematically depicted in Fig. 3.1

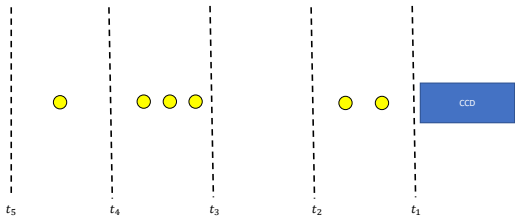


***Figure 3.1:*** *Schematic of a photon detection experiment of a coherent light source. The yellow circles are photons.*

Assuming a coherent light beam such as a laser, we can now ask what the probability $\rho(n)$ of detecting $n$ photons within a time $T$ is. First, divide $T$ into $N$ smaller time bins so each time bin contains at most one photon. $\rho(n)$ Is then given by the probability of finding $n$ time bins with a photon and $N-n$ timebins without a photon. This probability is given by the binomial distribution:

$$\rho(n) = \frac{N!}{n!(N-n)!}\left(\frac{\overline{n}}{N}\right)\left(1-\frac{\overline{n}}{N}\right)^{N-n} \tag{3.1}$$

where $\overline{n}$ is the average number of photons in time $T$. We then take the limit of $N \to \infty$, which after some intermediate steps gives:

$$\rho(n) = \frac{\overline{n}^n}{n!}e^{-\overline{n}}, \quad n = 0, 1, 2, ... \tag{3.2}$$

The fluctuations in the photon number are thus given by the Poisson distribution.



Version of July 24, 2023– Created July 24, 2023 - 13:47

## 3.2 Statistics of the experiment

In the 2AFC test the accuracy $A$ of choosing the correct interval and the probability $P$ of perceiving the light pulse are related as:

$$A = \frac{1}{2}(1 + P) \tag{3.3}$$

Note that the accuracy has a lower limit of $\frac{1}{2}$ since random guesses will be right 50% of the time. The accuracy of a subject of detecting a light pulse with photon number distribution $\rho_n$ for a constant source is given by [3]:

$$\begin{aligned} A(I_s) &= \sum_{n=0}^{\infty} a_n \rho_n(I_s) \\ &= 1 - \sum_{n=0}^{\infty} (1 - a_n)\rho_n(I_s) \\ &\approx \sum_{n=0}^{\infty} 1 - \sum_{n=0}^{n_{\max}} (1 - a_n)\rho_n(I_s) \end{aligned} \tag{3.4}$$

where $a_n$ is the accuracy for exactly $n$ photons, $\rho_n(I_s)$ is the probability that a source with settings $I_s$ emits $n$ photons. The infinite sum is terminated by assuming that a stimulus with more than $n_{\max}$ photons is always detected or when $\rho_m \approx 0$ with $m > n_{\max+1}$. Now the distribution of a Poissonian light source can be filled into Eq. 3.4 to yield the following accuracy:

$$A(\overline{n}) = 1 - e^{-\overline{n}} \sum_{n=0}^{n_{max}} (1 - a_n) \frac{\overline{n}^n}{n!} \tag{3.5}$$

where $\overline{n}$ is the mean number of photons per light pulse. In the experiment $A(I_s)$ is measured and $\rho_n(I_s)$ can be chosen. Equation (3.5) can then be fitted to the measured data to obtain $\vec{a} = [a_0, a_1, ..., a_{n_{max}}]$, which will give the sensitivity for $n$ photons. For the exact statistical details and simulations of the experiment, see [3].

## 3.3 Maxwellian view

In the previous two chapters, the nature of the light source and the statistical background of the experiment were discussed. The next two sections address the practical side: how can we direct the photons on the correct location on the retina? Under normal circumstances, our eye accommodates



Version of July 24, 2023– Created July 24, 2023 - 13:47

incoming light to form images onto the retina. This poses two challenges for the experiment. First, the angular orientation of the eyeball and secondly the accommodation of the lens. To conquer the first issue, we propose to use a fixation light. For the second issue, the so-called Maxwellian view (MV) will be employed, see Fig. 3.2.

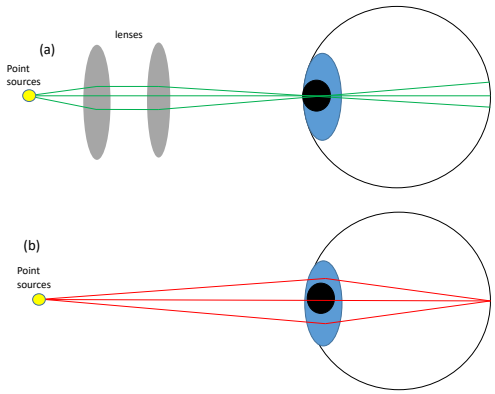


***Figure 3.2:*** *The light path for the Maxwellian view (a) and normal view (b). Note that the light path is unperturbed in the MV.*

In the MV, the light beam is focussed onto the lens. Up to first order, the light beam is unperturbed by the lens, which makes targeting a specific spot on the retina a lot easier. Additionally, the focal length of the eye will no longer influence the experiment. Using the MV also ensures that the image size on the retina remains constant, independent of the accommodation of the lens.

## 3.4 Gaussian beam

Propagating light can have several spatial distributions, called modes. The mode used in this experiment is the $TEM00$, or fundamental Gaussian mode which has, as the name suggests, a Gaussian intensity profile. Gaussian beams have several properties that make them advantageous to use in optical experiments [33]. These include the property that a Gaussian beam remains Gaussian when it propagates (in the paraxial limit), even when passing through lenses. The beam divergence is minimal and Gaussian beams can also be tightly focussed to the optical diffraction limit. The

intensity pattern of the Gaussian mode is given by [34]:

$$I(r,z) = \frac{2P}{\pi w(z)^2} e^{-2\frac{r^2}{w(z)^2}} = I_0 \left(\frac{w_0}{w(z)}\right)^2 e^{\frac{-2r^2}{w(z)^2}} \tag{3.6}$$

where $w(z)$ is the beam radius where the intensity is $1/e^2$ of the maximum intensity, and $r$ radial distance from the center axis and $z$ is the axial distance from the focus. $w_0$ Is the beam waist, which is the beam radius in the focus and $I_0 = \frac{2P_0}{\pi w_0^2}$ with $P_0$ the total power of the beam. The definition of the beam waist and the beam radius can vary dependent on the specific literature. The definitions used in this thesis are shown in Fig. 3.3.

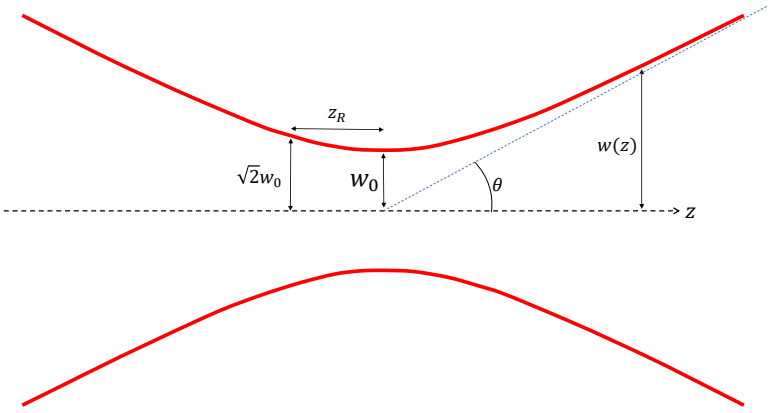


***Figure 3.3:*** *Gaussian beam radius $w(z)$ as a function of the distance $z$ along the beam, which forms a hyperbola. With $w_0$ the beam waist, $z_R$ the Rayleigh length and $\theta$ the divergence angle*

The beam radius of a Gaussian beam can be described by the following formula:

$$w(z) = w_0 \sqrt{1 + \left(\frac{z}{z_r}\right)^2} \tag{3.7}$$

where $z_R$ is the Rayleigh length, defined as:

$$z_R = \frac{\pi w_0^2}{\lambda} \tag{3.8}$$

The Rayleigh length is an important property of the beam, it describes the approximate length of the focus and the ray description breaks down within the Rayleigh length [35]. Within the Rayleigh length, the beam

radius remains nearly constant, whereas the beam divergence becomes increasingly more linear when going further away from the beam focus. The expansion of the propagating beam can be characterised by the divergence angle $\theta$. In the far-field region ($z \gg z_R$), the beam divergence is defined as:

$$\theta = \frac{\lambda}{\pi w_0} \tag{3.9}$$

Chapter 4

# Methods and materials

Now that the relevant theory and experimental principles were presented, we can shift our attention to the realisation of the experiment. The requirements for the setup can be divided into two main sections. First, the eye has to be positioned at the focus of the beam and it has to remain stable there. The second requirement is connected to the beams and includes properties such as the position of the focus and the divergence angle. The angle of incidence of the beam with the eye has to be adjustable to target the proper area on the retina. In the first section, the part of the setup that keeps the eye stable and in a specific spot is discussed, in the second section we discuss the part of the setup that creates a beam with the proper properties. In the last two sections, we discuss the methods used to characterise the beam radius and the simulations used to analyse the beam paths within the eye.

## 4.1 Setup of the optical arms

This part of the setup focuses the light at the eye lens and ensures that the photons hit the lens of the eye at the proper angle. It consists of a fixation arm and a target arm. The fixation arm is used to send a fixation light onto the eye. The test subject is asked to focus their eye on this beam during the experiment. This ensures the correct orientation of the eye. The target arm is used to send the few-photon light pulses onto the highest-density rod area on the retina. For the fixation beam, we use a standard 500 nm LED, which can be attenuated to achieve few-photon light pulses. Fig. 4.1 gives an overview of the different components.

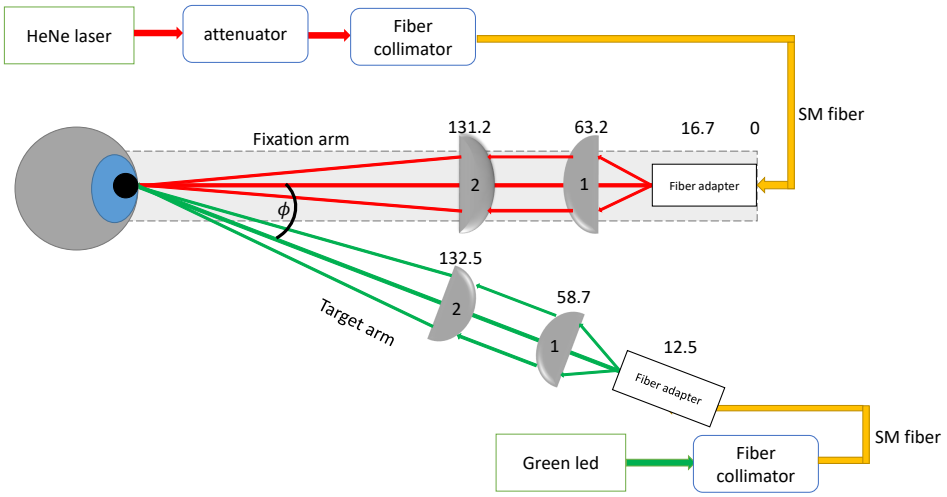


***Figure 4.1:*** *Schemetic overview of the optical setup of the experiment. Both optical systems consist of a light source, a 50 mm lens denoted with a* 1 *and a 300 mm lens denoted with a* 2*. The angle $\phi$ between the fixation arm and the target arm can be changed by moving the target rail. The orientation of the plano-convex lenses is chosen to minimise aberration. The number above the components gives their position in mm, as defined in the text. The pivot point between the rails is at the intersection point of the beams. In this figure, the lens of the eye is placed at the pivot point.*

Both light sources are coupled into a single mode fiber[1] using a fiber collimator. The light source for the fixation arm is a 632.8 nm-HeNe laser and the light source for the target arm is a green LED. The other end of the single mode fiber is placed in the fiber adapter.[2] For the target arm, the fiber adapter is placed in a translation mount.[3] The fiber adapter and the lenses are all placed on rails[4]. On each rail, two lenses are mounted. The first lens is a plano-convex lens[5] with a focal length of 50 mm, which collimates the beam from the fiber. The second lens is a 300 mm lens[6] used to focus the beam onto the eye. The exact equipment used to hold the lenses and the dimensions of this equipment can be found in Appendix A.

[1] P1-460A-FC-2 for target and FS-SN-3224 for fixation
[2] SM1FC from Thorlabs
[3] LM1XY from Thorlabs
[4] RLA450/m dovetail rails from Thorlabs
[5] LA1131-AB: N-BK7 from Thorlabs
[6] LA1484-AB: N-BK7from Thorlabs

In the experiment, the angle $\phi$ has to be adjustable around a certain pivot point. During the experiment, the eye will then be positioned at this pivot point. The pivot point is created by placing the target rail on the fixation rail and fixing them together with a screw. The fixation rail is then attached to an optical board.
For the remainder of this report, the distance values of elements on the rails are defined relative to the side of the rail where the fiber adapters are placed. The origin is thus defined at the start of the rail, denoted with a 0 in Fig. 4.1. In this definition, the pivot point is at position 426 mm, which is thus the position where both beams will be focused and where the eye will be placed during the experiments.

### 4.1.1 Lens alignment

The correct alignment procedure of both rails is the same and is shortly explained in this section. The first step is to make sure the beam from the fiber adapter is aligned with the rails. This is done by initially placing the single mode fiber into a fiber collimator, instead of the fiber adapter. A CCD camera[7] is then moved over the rails, and the transverse position of the beam should remain constant. The two lenses are then one by one placed on the rails. The lenses are correctly aligned if the position of the beam in the transverse plane to the beam remains unchanged. The fiber collimator can then be replaced with the bare fiber adapter.
Next, the position of the lenses has to be determined. Behind the 50 mm lens, the beam should be collimated. This is confirmed by moving the CCD away from the lens, and checking if the size of the beam stays equal. Finally, the CCD is placed at 426 mm and the position of the 300 mm lens is changed until the focus is at the CCD. The exact positions of the lenses are displayed in Fig. 4.1.

## 4.2 Eye stabilisation

The second part of the setup ensures the stability of the head of the test subject. To keep the head stable a headlock is used, see Fig. 4.2

[7] Spiricon SP620U

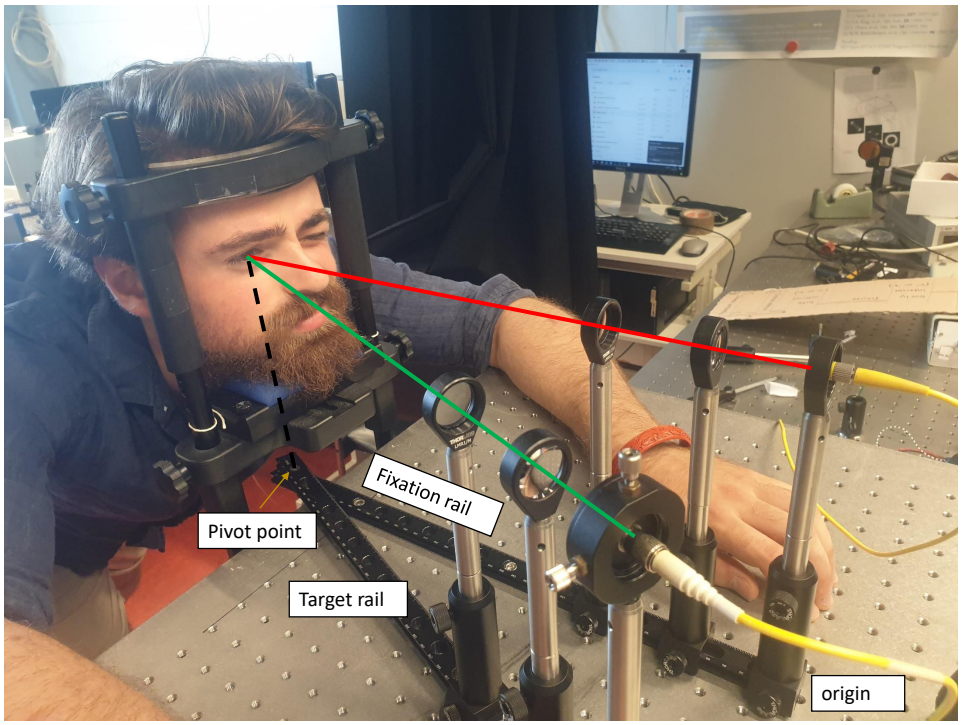


***Figure 4.2:*** *Picture of the current setup. The fixation beam is shown in red and the target beam is shown in green*

The orientation of the eye is kept stable with a dim fixation light. For the setup to be adaptable for each test subject it has to have 3 degrees of freedom, one for each spatial dimension. The eye can be moved up and down using the chin rest on the headlock, the other two degrees of freedom were adjusted manually. An important part of the experiment is to determine whether the setup can keep the position of the head and the orientation of the eye stable.

## 4.3 Methods to define the beam radius

To analyse the beam properties, the beam radius has to be determined at different positions of the beam. For this research project, three different methods to determine the beam radius are developed and used.

### 4.3.1 Cross sections

The most straightforward way to determine the beam radius is to characterise cross-sections from the measured intensity profile. The cross-sections are taken horizontally or vertically through the position of the highest intensity. The indices left and right of the maximum which are closest to $1/e^2$ the maximum intensity are determined. The distance between these points gives the beam diameter, which can easily be converted to the beam radius. This method will be referred to as the ”cross-section method”.

### 4.3.2 Circle fit method

The second method is similar to the previous one but uses the 2D array. First, all the indices that have an intensity of $1/e^2$ that of the maximum intensity are marked. Since there will be no indices where the data is exactly $1/e^2$ the maximum intensity, all values within a certain range around this fraction are taken. The optimal value for this range is manually determined with trial and error. Then a circle is fitted through these indices. The fit value of the circle radius now gives the beam radius. This is illustrated in Fig. 4.3. This method will be referred to as the ”circle fit method”.

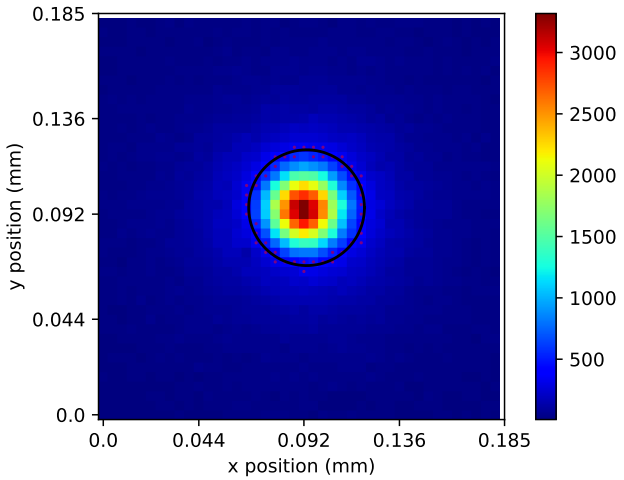


***Figure 4.3:*** *Example of the circle fit method on the target beam at 436 mm. The purple dots are all indices with a value of 13.5 % ± 4% of the maximum value.*

### 4.3.3 D86 method

The previous two methods work well for beams that resemble Gaussians, but they can not be used for the more complex beams that are observed during this experiment. To overcome this issue, we use the D86 method to determine the beam radii for the more complex parts of the beam [36]. This method defines the beam radius by determining a circle which encloses 86.5% of the total power of the beam. The value of 86.5% comes from the fact that the power of a Gaussian beam integrated from the peak to the beam radius gives 86.5% of the total power of the beam. This circle then gives the beam radius. For this research project, this method will be used with 1D cross-sections. Notice that for a perfect Gaussian beam, all three methods give the same beam radius.

## 4.4 Ray tracing simulations of the eye

For this experiment, it is important to know how light is refracted by the different components of the eye. This will give a procedure to theoretically determine whether certain parts of the setup are precise enough to do further experiments. A simulation of the eye was made by the thesis supervisor Tom van der Reep, using the ray tracing software opticalraytracer. The parameters of the different components of the eye are taken from [37].
The diameter of the beam after the 50 mm lens is 7.8 mm, measured on the fixation arm since the intensity of the beam of the target arm was too low to perform a measurement. A rough estimation of the expected beam diameter can be made using the formula for the divergence angle $\theta_{\text{SM}}$ of a single mode fiber[38]:

$$\theta_{\text{SM}} = \frac{2 \cdot \lambda}{\pi \cdot \text{MFD}} \tag{4.1}$$

where $\lambda$ is the wavelength and MFD is the mode field diameter. The MFD of the optical fiber is $4\mu$m. Taking a value between the fiber adapter and the first lens of 50 mm, this gives a diameter of

$$50 \cdot \tan(\theta_{\text{max}}) = 50 \cdot \tan\left(\frac{2 \cdot 632.8 \cdot 10^{-6}}{\pi \cdot 4 \cdot 10^{-3}}\right) = 5.0\text{mm} \tag{4.2}$$

This gives a diameter of around 10 mm, which corresponds reasonably well with the measured value. The measured diameter of 7.8 mm will be used to set the outer rays in the simulation. The basic setup for the

simulation is displayed in Fig. 4.4. The positions and angles of the lens and the source can now be changed to perform different simulations.

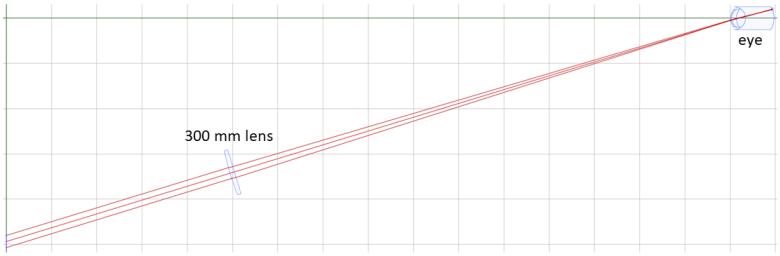


***Figure 4.4:*** *Exemplary ray tracing simulation showing the 300 mm lens and the eye.*

Chapter 5

# Analysis of the beams

Now that the setup and methods have been discussed, two important properties of the beam are determined: the exact position of the focus and the beam divergence. In this chapter, we will focus on the target beam, hereafter referred to as 'the beam' unless otherwise specified. The beam profile is measured at different distances around the beam focus. Using the methods described in Chapter 4 the exact divergence of the beam and position of the focus are determined. These results are used to simulate the expected beam trajectory in the eye. The simulations are then used to conclude if the setup can be used for experiments using human observation.

## 5.1 Characterising the beam

The intensity profile of the beam is measured between 396 and 456 mm. A part of these measurements is displayed in Fig. 5.1.

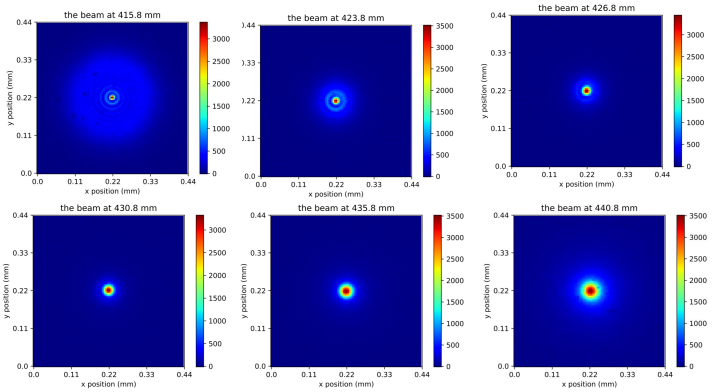


***Figure 5.1:*** *The intensity pattern of the beam on the target arm at different positions. The colour scale indicates the intensity in counts.*

Before 427 mm the intensity of the beam shows clear ring patterns. These rings will be further discussed in section 5.4. The 'cross section' and 'circle fit' methods can only be used when working with beams that can be reasonably well approximated by a Gaussian beam profile. To correctly determine the position of the focus we first use the D86 method. Then the other two methods will be used in the region behind the focus. The results with fits are shown in Fig. 5.2.

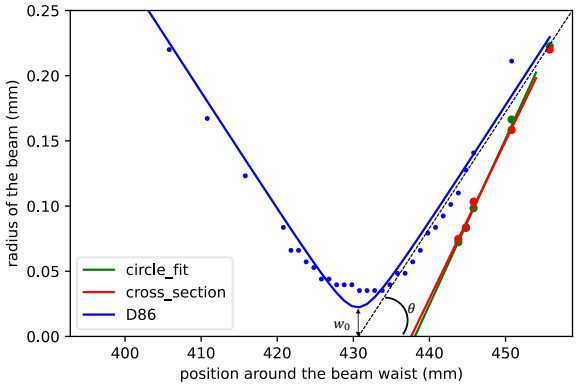


***Figure 5.2:*** *The beam radii with fits calculated for the three different methods. The beam waist and beam divergence are noted in the figure. The stepwise data points for the beam radius around the focus for the D86 method are caused by the limited pixel size.*

Now we will discuss how the beam divergence and the exact position of

the focus are determined from these measurements.

### 5.1.1 Analysis

Because the D86 method is the only method that can be used for more complex beam profiles, we first use this method to determine the position of the focus. This is done by fitting the data to the formula for the beam radius:

$$w(z) = w_0 \cdot \sqrt{1 + \left( \frac{\lambda \cdot (z - z_0)}{\pi \cdot w_0^2} \right)^2} \tag{5.1}$$

The fit parameter $w_0$ gives the beam waist and $z_0$ will give the focus position. Equation (3.8) and Eq. (3.9) are used to calculate the rayleigh length and the beam divergence.
Behind the focus, the beam profile starts to resemble a Gaussian, which means the circle fit and cross section method can be used for analysis. To compare the measured beam with an ideal Gaussian, a Gaussian fit of the beam is made. An example is given in Fig. 5.3, where the measured beam, the fit and their difference at 440 mm are shown. Note that the measured intensity profile has a narrower peak than the perfect Gaussian, this explains the lower values for the beam radii for the circle fit and cross section method.

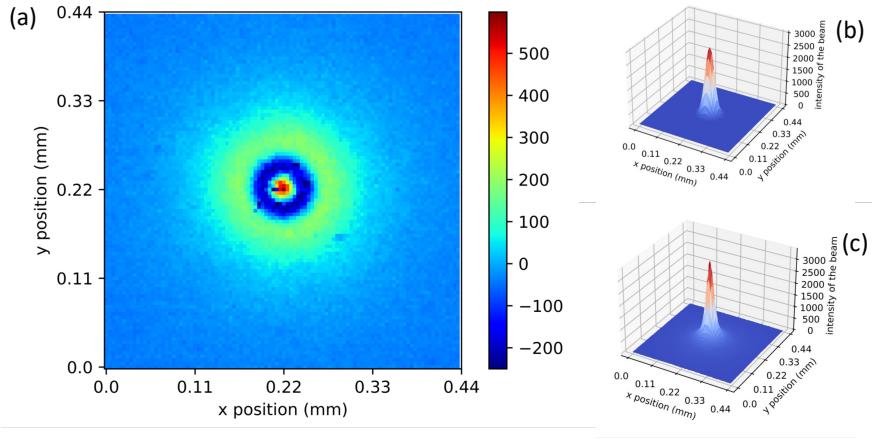


***Figure 5.3:*** *Panel (a) Shows the difference between experimental data and the Gaussian fit. (b) shows the Gaussian fit and (c) shows the experimental data.*

To determine the divergence the beam radii in the far-field region are calculated. After 455.8 mm, the beam becomes too weak to perform reasonable measurements. The calculated radii are fitted to the following function, using that in the far-field region the beam radius $w(z)$ converges to a linear function:

$$w(z) = a \cdot (z - b) \tag{5.2}$$

where $a$ is the divergence angle and $b$ gives the position of the focus. The results from both methods and their fits are displayed in Fig. 5.2. The point where this function intersects with the propagation axis of the beam is the focal point. From the divergence angle, the beam waist and Rayleigh length can then be calculated using Eq. (3.9) and Eq. (3.8). The results are shown in Table 5.1

| | focus position (mm) | beam divergence (rad) | Rayleigh length (mm) | beam waist(mm) |
|---|---|---|---|---|
| circle fit | $438.1 \pm 0.3$ | $(1.27 \pm 0.03) \times 10^{-2}$ | $0.98 \pm 0.05$ | $(1.25 \pm 0.03) \times 10^{-2}$ |
| cross section | $437.6 \pm 0.3$ | $(1.21 \pm 0.03) \times 10^{-2}$ | $1.09 \pm 0.05$ | $(1.32 \pm 0.03) \times 10^{-2}$ |
| D86 | $430.6 \pm 0.3$ | $(0.72 \pm 0.01) \times 10^{-2}$ | $3.1 \pm 0.1$ | $(2.22 \pm 0.04) \times 10^{-2}$ |

***Table 5.1:*** *The obtained values and statistical errors for the different properties characterising the target beam with the three different methods. The standard deviations of the fits are used to determine the statistical errors.*

### 5.1.2 Simulations

For the Maxwellian view, the beam has to be focussed at the lens. Both the movement of the eye and the imperfect alignment in the setup causes the focus to be either before or behind the lens of the eye. The simulations are used to determine the influence this offset has on the beam path inside the eye. Both the situation where the focus is at the lens and where the focus is 12 mm behind the lens are simulated. The results can be seen in Fig. 5.4

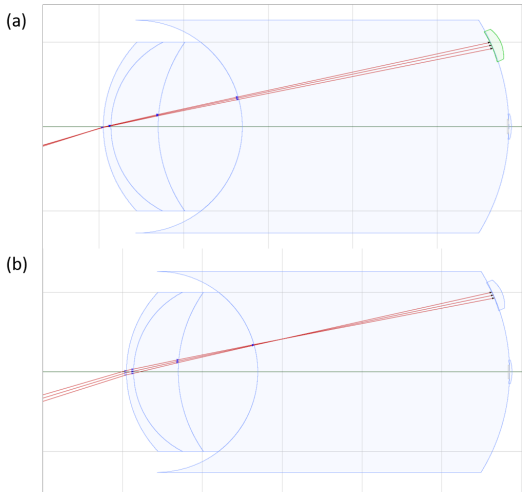


***Figure 5.4:*** *Raytracing simulations where the focus is perfectly positioned at the lens of the eye (a), and for the focus positioned 12 mm behind the lens (b). We observe a negligible displacement of the spot on the retina.*

The simulations show that the beam paths inside the eye are very similar for both the perfect and imperfect aligned focus positions. This is supported by self-made observations that the diameter of the beam does not significantly change when the lens of focal length 300 mm is moved multiple centimetres to the front or to the back.
To test the influence of the beam divergence on the area on which photons will hit the retina two situations are simulated: one with the experimentally measured divergence and one with a divergence twice that value. The average divergence angle of the three methods is taken, which gives a divergence of 0.011 rad. The radius of the beam in the simulation is adjusted to match this divergence. The two simulations are displayed in Fig. 5.5.

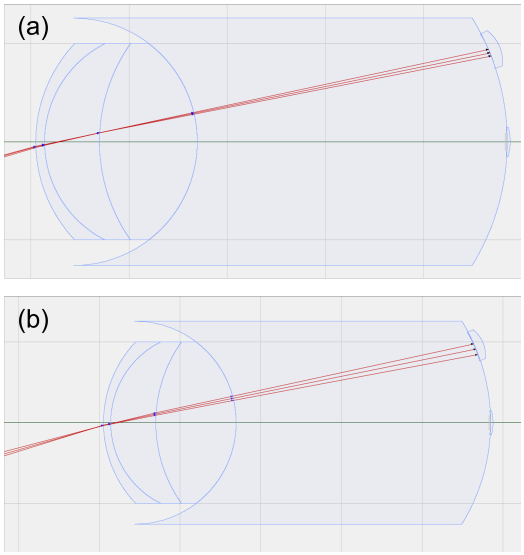


***Figure 5.5:*** *Raytracing simulations with a beam divergence equal to the experimental value (a), and for the beam divergence twice that value.*

The angle of the beam on the retina is calculated using ImageJ. The total angle of the beam on the retina for a divergence angle of 0.011 rad is 0.017 rad and for 0.022 rad it is 0.030 rad.

### 5.1.3 Discussion

The position of the focal point is determined in three different ways. All obtained values are shown in Table 5.1. The discrepancy between the D86 method and the other two is most likely caused by the fact that we used the assumption that the beam was a perfect Gaussian for the circle fit and the cross-section method. To analyse this further the difference between the Gaussian fit and the actual data was calculated, see Fig. 5.3. This shows the beams are more sharply peaked than perfect Gaussian, which explains the smaller beam radii as compared to those obtained with the D86 method. The real position of the focus will lay closest to the value found with the D86 method.
The influence of the axial offset of the position of the focus has been demonstrated in Fig. 5.4. From the simulations, we conclude that an axial accuracy of 12 mm for the focus position is enough to perform reliable experiments.
To control whether the found divergence angles are realistic we performed a simple calculation. The beam radius before the 300 mm lens is 3.88 mm,

calculated with the circle fit method. At the focus position 300 mm after the lens, we obtain:

$$\theta = \arctan\left(\frac{3.88}{300}\right) = 1.3 \cdot 10^{-2} \text{ rad}$$

This lies very close to the average divergence angle of $1.1 \cdot 10^{-2}$ rad found in the experiment. From the simulation, we found that a beam with a divergence angle of 0.011 rad has an angular diameter on the retina of 0.017 rad. This is around a factor 5 smaller than the target area. It can thus be concluded that the current beam divergence is small enough to do actual experiments with humans.

## 5.2 Characterisation of the fixation beam

The above measurements are also done for the fixation arm, this will give an interesting comparison between LED and laser light as inputs for a single mode fiber. The methods to analyse the beam are exactly the same as for the target arm. A part of the measurements is displayed in Fig. 5.6.

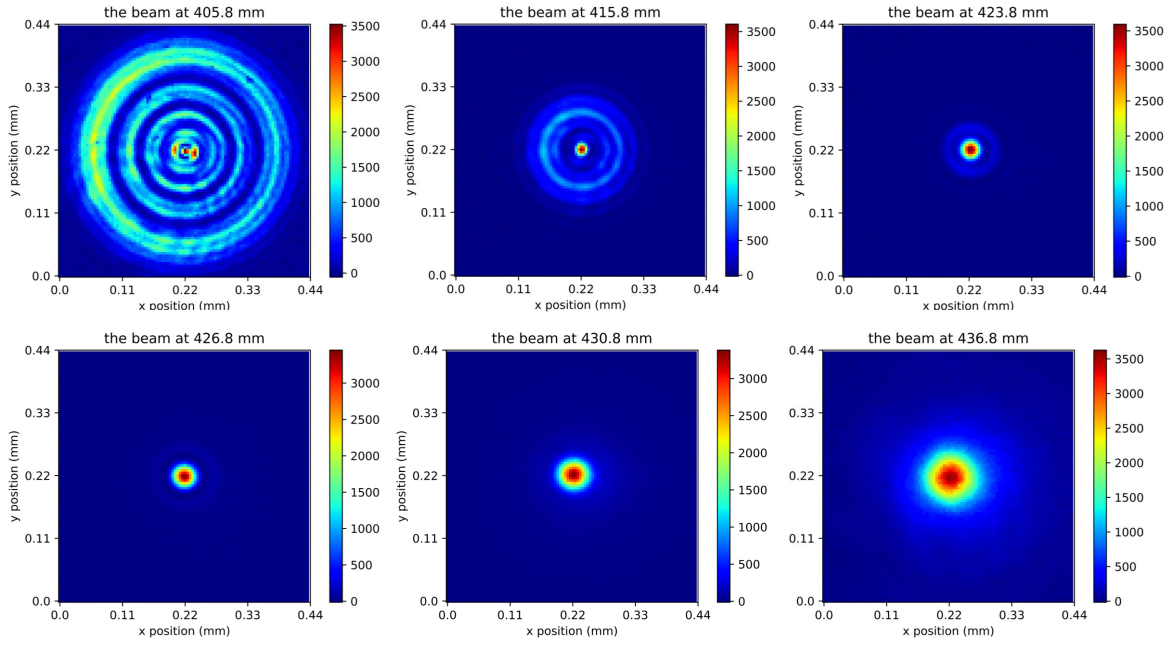


***Figure 5.6:*** *The intensity patterns of the fixation beam. The colour scale shows the intensity in counts of the CCD.*

Before the focus, the beam intensity again shows a ring pattern. For the laser input, the ring pattern is much clearer and the peaks and the minima and maxima of the rings are well separated. The calculated beam radius $w(z)$ and fits are shown in Fig. 5.7.

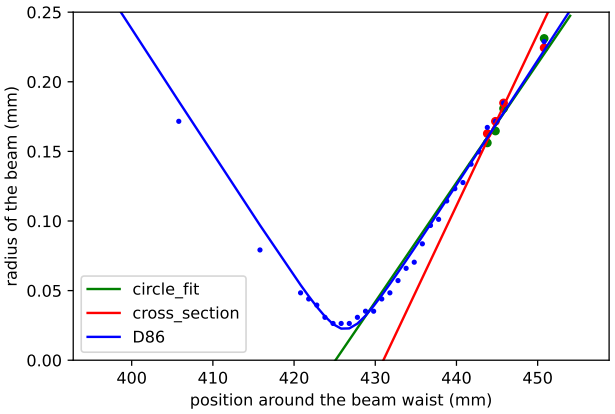


***Figure 5.7:*** *The beam radii with fits for the fixation beam calculated for the three different methods.*

The relevant values are calculated from the fit values and are displayed in Table (5.2).

| | focus position (mm) | beam divergence (rad) | Rayleigh length (mm) | beam waist(mm) |
|---|---|---|---|---|
| circle fit | $425 \pm 2$ | $(0.85 \pm 0.08) \times 10^{-2}$ | $2.9 \pm 0.5$ | $(2.4 \pm 0.2) \times 10^{-2}$ |
| cross section | $431 \pm 2$ | $(1.2 \pm 0.1) \times 10^{-2}$ | $1.4 \pm 0.2$ | $(1.7 \pm 0.1) \times 10^{-2}$ |
| D86 | $426.3 \pm 0.2$ | $(0.86 \pm 0.09) \times 10^{-2}$ | $2.6 \pm 0.5$ | $(2.33 \pm 0.02) \times 10^{-2}$ |

***Table 5.2:*** *The obtained values and statistical errors for the different properties characterising the fixation beam with the three different methods.*

The average beam waist for the 632.8 nm HeNe laser is 1.5 times larger than that of the beam waist of the 500 nm LED. Under the approximation that the beam at the lens is around the same size as the lens, the beam waist can be approximated by:

$$w_0 = \frac{2\lambda f}{\pi d} \tag{5.3}$$

with $\lambda$ the wavelength, $f$ the focal length of the lens and $d$ the diameter of the lens [35]. Assuming both beams have the same diameter at the lens with a focal length of 300 mm we do expect a larger beam waist for the laser.

## 5.3 Angle between the beams

Now that the focus position and the divergence of the beam in the target arm are known, the two systems can be combined as explained in Chapter 5. To check the correct alignment of the two beams the CCD is placed on the fixation real and the beams are measured on 3 different positions: 420 mm, 426 mm and 440 mm. For each measurement, the distance between the peaks is determined. The two beams at position 426 mm are shown in Fig. 5.8

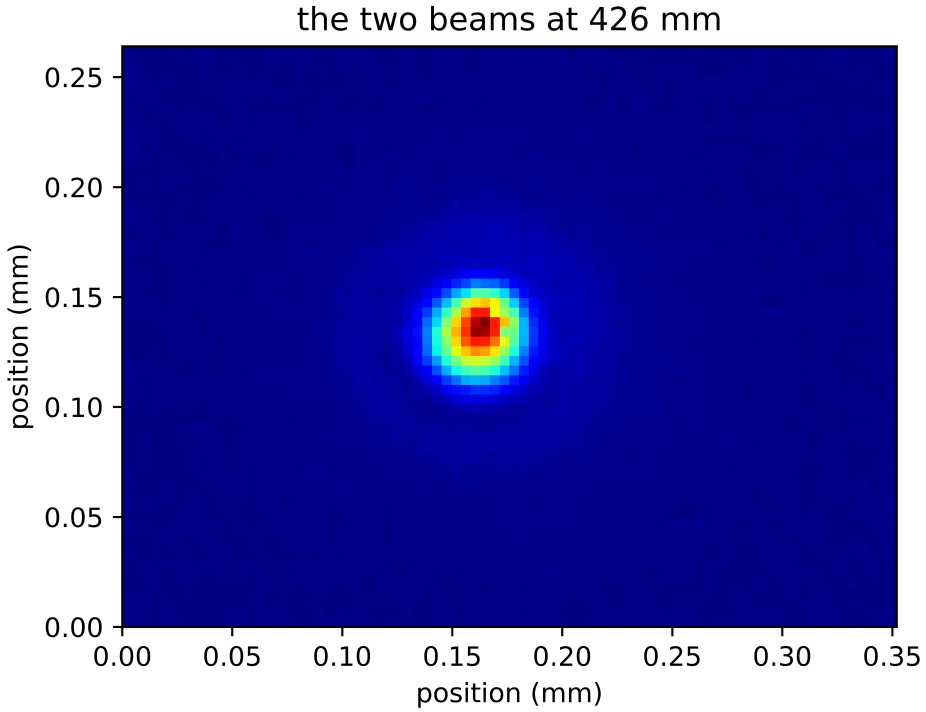


***Figure 5.8:*** *Crossing point of the two beams at 426 mm. Note that the two beams are no longer separable.*

From Fig. 5.8 one can clearly see they overlap very well, with a precision well below one mm. Also note that we do not see any interference, as expected for two beams of different wavelengths.
Since the positions of the measurements and the distance between the beams are known the angle can be easily calculated. The angle between the beams before the crossing point is 0.34 rad and the angle after the crossing is 0.29 rad. This discrepancy probably originates from impre-

cise measurements. The measured angle between the rails was 0.32 rad. An important question now is what the influence of a small uncertainty in the beam angle on the experiment is. To give an indication the error caused by an offset of 0.03 rad will be quickly calculated. Since the area of highest rod density lies in a ring 0.17 and 0.3 rad [12, 39], an error of 0.03 rad should not pose a big problem. It will be important, however, to keep in mind when analysing the results from the first tests done with human observation.

## 5.4 Ring pattern

The exact cause of the ring pattern is unknown at this point. Interestingly, the pattern strongly resembles the Laguerre-Gaussian mode. To show this resemblance the $TEM_{01}$ mode is made with the Beamgage software, see Fig. 5.9.

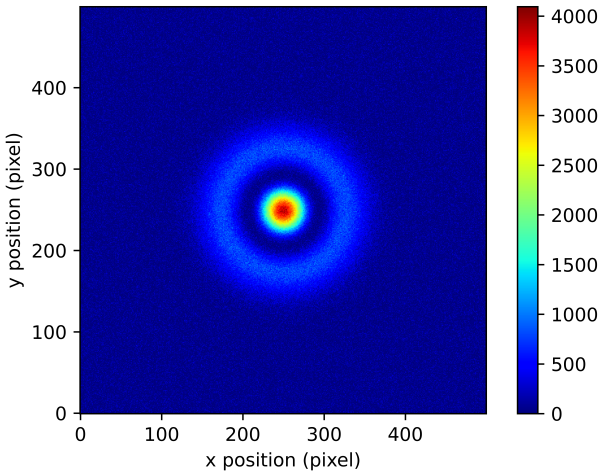


***Figure 5.9:*** *The $TEM_{01}$ mode for the Laguerre-Gaussian modes. Gaussian noise is added to make the figure more realistic.*

When comparing this to the fixation beam at position 415.8 mm, the similarities are very obvious. The pattern of the fixation light looks a lot like an airy disk. An airy disk is created when a circular aperture is uniformly illuminated. The resulting diffraction pattern is called an airy disk [40]. Since lenses have a finite diameter they will act as an aperture. Both the experimentally measured and theoretically calculated diameters of the beam at

the lenses are smaller than the lenses however so this should not be an issue. To test this further a 1 cm aperture was placed in the middle between the fiber adapter and the 50 mm lens and in the middle between the 50 mm lens and the 300 mm lens. The result is shown in Fig. 5.10.

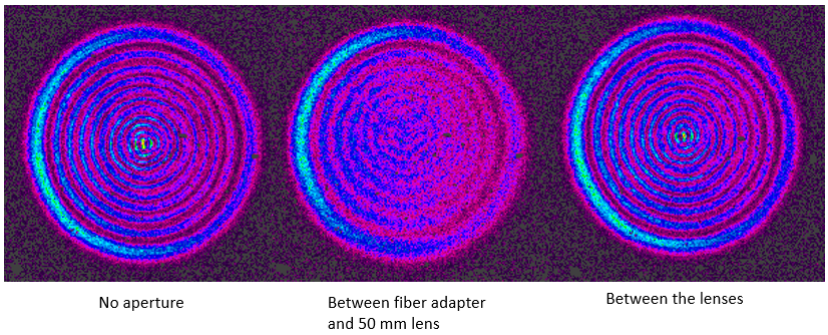


***Figure 5.10:*** *The intensity pattern of the fixation beam for the different aperture positions.*

The ring pattern remains visible for all positions of the aperture. Note however that the small centre peak disappears when placing the aperture between the lenses.
Therefore, the ring pattern is most likely caused by spherical aberrations at the lenses [41]. Spherical aberrations are caused by the fact that parallel rays, which go through a lens at different distances from the optical axis will be refracted differently, see Fig. 5.11.

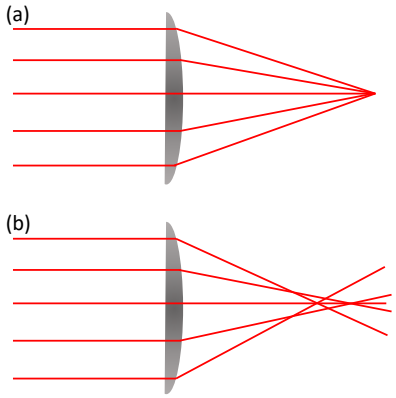


***Figure 5.11:*** *An ideal lens without spherical aberrations (a) and a realistic lens with spherical aberrations (b).*

The rings can be explained by spherical aberration, but one question re-

mains: why is the ring pattern very clear before the focus and disappears almost completely after the focus? A slightly different intensity pattern before and after the focus can be expected [42], we cannot explain however why the effect is so strong in these experiments.

## 5.5 Conclusion

The position of the focus and the divergence of the beam have been determined in 3 different ways. The beam paths in the eye considering these measurements have been simulated and their influence during the experiment is discussed. The impact of the offset of the position of the focus and the divergence is insignificant enough that the first reliable experiments on humans can be done.

Chapter 6

# First tests using human observation

Now that the focus position and the divergence of the beams are known, the setup is used for the first tests with humans. In these tests, the dimensions of the optic disc are determined. The determined dimensions are then compared to the dimensions given in the literature. From this, possible modification of the beam path by refraction at the lens can be determined. The statistical errors of the measurements are calculated and used to determine the stability of both the position and the orientation of the eye during the experiment. The determined refraction and stability are then used to discuss whether the current setup is suitable to perform the final experiment.

## 6.1 Method and results

### 6.1.1 Experimentel procedure

The subject was asked to place their head in the headlock, this is shown in Fig. 4.2. Both the fixation and target beams are on. During the experiment, the subject fixates their right eye on the fixation light and their left eye was covered with an eye patch. The angle $\phi$, as defined in Fig. 4.1, between the target rail and fixation rail is then slowly alternated. One measurement happens in the following way. $\phi$ is made small so both beams are visible. Then $\phi$ is increased until the target beam disappears, i.e. the beam is at the optic disc. The position where this happens is noted on the optical

board. After the position is noted $\phi$ is further increased till the target light is again visible, i.e. the target beam is no longer at the optic disc. These measurements are repeated several times. During a set of measurements, the subject's right eye is continuously fixated. A picture of the optical board with the noted angles is made and the angles are measured using the ImageJ program.

### 6.1.2 Results

The first experiments were done with two subjects. Both subjects were males between 20 and 30 years old without any known eye deficiencies. The experimental values are shown in Table 6.1 and 6.2.

| measurement | temporal angle (rad) | nasal angle (rad) |
|---|---|---|
| 1 | 0.216 | 0.316 |
| 2 | 0.224 | 0.316 |
| 3 | 0.228 | 0.324 |
| 4 | 0.233 | 0.332 |
| 5 | 0.233 | 0.337 |
| 6 | 0.237 | 0.337 |

***Table 6.1:*** *Measured angles of the temporal side and nasal side of the optic disc for subject one. The nasal side is the side of the retina closest to the nose and the temporal side is the side closest to the ear*

| measurement | temporal angle (rad) | nasal angle (rad) |
|---|---|---|
| 1 | 0.248 | 0.316 |
| 2 | 0.251 | 0.323 |
| 3 | 0.255 | 0.323 |
| 4 | 0.249 | 0.333 |
| 5 | 0.260 | 0.342 |

***Table 6.2:*** *Measured values for the angle of the temporal side and nasal side of the optic disc for subject two.*

The averages over the temporal and nasal angles are taken to determine the dimension of the optic disc. From the statistical error, we can then make conclusions about the stability of the head. The determined dimensions and statistical errors are shown in Table 6.3.

| | subject one | subject two |
|---|---|---|
| nasal (rad) | $0.327 \pm 0.009$ | $0.327 \pm 0.009$ |
| temporal (rad) | $0.229 \pm 0.007$ | $0.253 \pm 0.004$ |

***Table 6.3:*** *Averages of the temporal and nasal side of the optic disc with statistical errors.*

From these determined values, the horizontal size of the optic disc can be calculated. For subject one this size is $0.10 \pm 0.01$ rad and for subject two it is $0.074 \pm 0.01$ rad. The centre of the optic disc for subject one is at 0.28 rad and for subject two at 0.29 rad. A set of measurements had a duration of approximately 3 minutes.

## 6.2 Discussion and conclusion

The distance between the fovea and the centre of the optic disc is $0.27 \pm 0.02$ rad and the optic disc has a horizontal width of 0.071 rad. The experimentally found values agree very well with the theoretical values. This confirms that the beam paths are largely unperturbed by the lens, showing that the arms can be used to target a specific spot on the retina. Note that the theoretical angular distances of the optic disc are measured from the fovea. We assumed here that the light from the fixation arm falls onto the fovea. This is justified by the fact that objects are imaged on the fovea when the eye fixates on the object [43].
The second goal of these experiments was to determine the stability of the eye in the headlock. The statistical error of the previous experiments can be used as a measure for this stability, assuming this statistical error arises from the movement of the head and the changing orientation of the eye. The average statistical error for the nasal and temporal measurements of the two subjects is 0.0073 rad. This is around the diameter of the optic disc, which is a lot smaller than the area of the highest rod density. From this, it could be concluded that the current setup is suitable to perform the final experiment. There are some important factors that have to be accounted for, however. During the experiments, the fixation light was continuously on, which gave the test subjects a way to manually keep their head stable. During the final experiment, the fixation light would ideally be off, which would make it significantly harder for test subjects to correctly reposition the head. Second, the experiments were done in a relatively short time span relative to the final experiment. Factors such as concentration loss and tiredness of the body to keep the head stable did not influence this

experiment, but they will be in the final experiment.
To conclude, the arms can be used to reliably target a specific spot on the retina. The headlock keeps the head stable enough in the current experiment, but more tests will have to be done to confirm if the headlock is suitable for the final experiment.

Chapter 7

# Conclusion and outlook

In this thesis, we described the first steps towards the realisation of an experimental setup in which detector tomography is used to determine the accuracy of human vision to few photon number states. A setup was built consisting of a headlock and two arms: a fixation arm and a target arm. The angle between the two arms is adjustable. The beams of both arms were characterised and two main properties were analysed: the exact position of the focus and the divergence angle of the beam. The beam paths in the eye were simulated and it is concluded that this setup can be used for accurate experiments using humans.
The first tests using human observation were done. The dimensions of the optic disc were measured and compared with the theory. The experimental values agreed with values found in the literature, so the current setup can be used to target the area of the highest rod density. However, these tests were done in dim light, which makes correct alignment easier for the test subjects. More experiments will be necessary to confirm the feasibility of the current setup. These include experiments over longer time spans and in completely dark rooms. Once these are completed the first real experiments determining the number of photons necessary to create visual perceptions can be done. With these experiments, the accuracy of humans perceiving single photons, and few photon states in general can be determined. This would open up new ways to test the fundamentals of quantum theory, such as bell tests with human observers.



Version of July 24, 2023– Created July 24, 2023 - 13:47

Appendix A

# Appendix

## A.1 A: Post holder equipment and dimensions

The exact positions of the lenses can't be read off directly since they are placed in other optical equipment. See Fig A.1 for all the equipment.

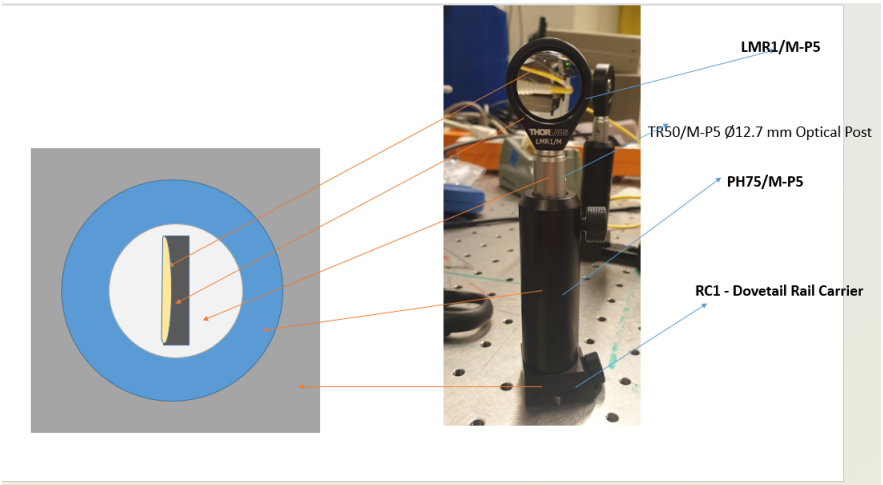


***Figure A.1:*** *Figure of the lens within the different optical equipment. This equipment is the same for all the lenses. The left side is a top view of the lens holder. This will be important for determining the exact position of the lenses*

The position of the lens holder is read of from the side rail carrier. The exact position of the lens is then determined using the dimensions shown in Fig. A.2.

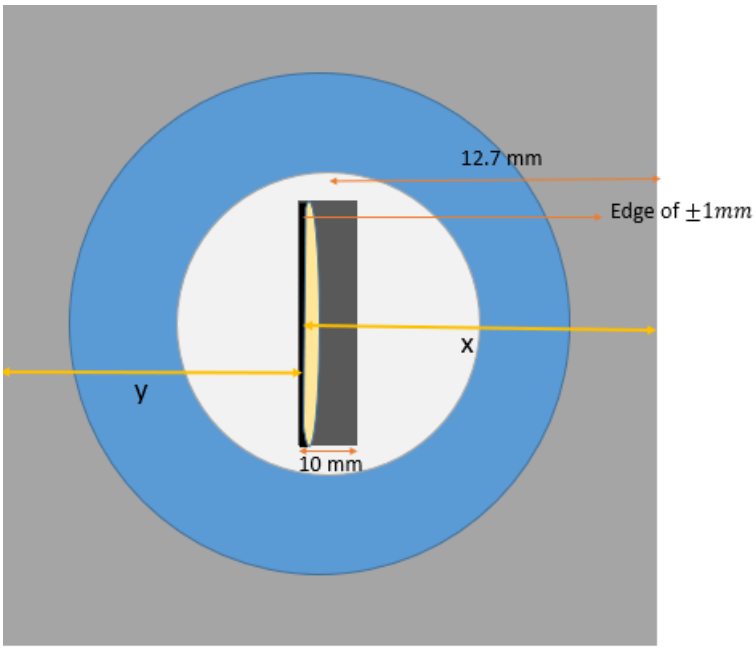


***Figure A.2:*** *Top view of the lens post, not to scale. The dimensions are taken from the Thorlabs site or measured with a caliper. The lens can be stationed on both sides of the lens mount, which determines if length x or length y will be used.*

Length x is 16.7 mm and length y is 8.7 mm.

# Acknowledgements

First and foremost I would like to thank my daily supervisor Wolfgang Löffler for his active support and involvement during this project. On the sporadic occasions that I did find your office door closed, I never had to wait long before getting an online answer to my questions. Second, I am thankful to my second supervisor Tom van der Reep for laying the foundations on which I could build this project and for guiding me during it. Lastly, I would like to express my gratitude to all the members of the quantum optics group. Thank you for your input during the group meetings, helping me with all the little stupid stuff, giving feedback on this thesis, and most importantly making the months I spent on this floor very enjoyable.

# Bibliography

[1] S. Hecht, S. Shlaer, and M. H. Pirenne, "Energy at the Threshold of Vision," *Science*, vol. 93, no. 2425, pp. 585–587, Jun. 1941. [Online]. Available: https://www.science.org/doi/10.1126/science.93.2425.585

[2] J. N. Tinsley, M. I. Molodtsov, R. Prevedel, D. Wartmann, J. Espigulé-Pons, M. Lauwers, and A. Vaziri, "Direct detection of a single photon by humans," *Nature Communications*, vol. 7, no. 1, p. 12172, Jul. 2016. [Online]. Available: https://www.nature.com/articles/ncomms12172

[3] T. H. A. Van Der Reep, D. Molenaar, W. Löffler, and Y. Pinto, "Quantum detector tomography applied to the human visual system: a feasibility study," *Journal of the Optical Society of America A*, vol. 40, no. 2, p. 285, Feb. 2023. [Online]. Available: https://opg.optica.org/abstract.cfm?URI=josaa-40-2-285

[4] J. S. Lundeen, A. Feito, H. Coldenstrodt-Ronge, K. L. Pregnell, C. Silberhorn, T. C. Ralph, J. Eisert, M. B. Plenio, and I. A. Walmsley, "Tomography of quantum detectors," *Nature Physics*, vol. 5, no. 1, pp. 27–30, Jan. 2009. [Online]. Available: https://www.nature.com/articles/nphys1133

[5] V. C. Vivoli, P. Sekatski, and N. Sangouard, "What does it take to detect entanglement with the human eye?" *Optica*, vol. 3, no. 5, p. 473, May 2016. [Online]. Available: https://opg.optica.org/abstract.cfm?URI=optica-3-5-473

[6] G. Fain and A. P. Sampath, "Rod and cone interactions in the

retina," *F1000Research*, vol. 7, p. 657, May 2018. [Online]. Available: https://f1000research.com/articles/7-657/v1

[7] F. Pan, A. Toychiev, Y. Zhang, T. Atlasz, H. Ramakrishnan, K. Roy, B. Völgyi, A. Akopian, and S. A. Bloomfield, "Inhibitory masking controls the threshold sensitivity of retinal ganglion cells: Inhibition controls ganglion cell sensitivity," *The Journal of Physiology*, vol. 594, no. 22, pp. 6679–6699, Nov. 2016. [Online]. Available: https://onlinelibrary.wiley.com/doi/10.1113/JP272267

[8] T. J. Cherry, J. M. Trimarchi, M. B. Stadler, and C. L. Cepko, "Development and diversification of retinal amacrine interneurons at single cell resolution," *Proceedings of the National Academy of Sciences*, vol. 106, no. 23, pp. 9495–9500, Jun. 2009. [Online]. Available: https://pnas.org/doi/full/10.1073/pnas.0903264106

[9] U. S. Kim, O. A. Mahroo, J. D. Mollon, and P. Yu-Wai-Man, "Retinal Ganglion CellsâDiversity of Cell Types and Clinical Relevance," *Frontiers in Neurology*, vol. 12, p. 661938, May 2021. [Online]. Available: https://www.frontiersin.org/articles/10.3389/fneur.2021.661938/full

[10] C. A. Curcio, K. R. Sloan, R. E. Kalina, and A. E. Hendrickson, "Human photoreceptor topography," *The Journal of Comparative Neurology*, vol. 292, no. 4, pp. 497–523, Feb. 1990. [Online]. Available: https://onlinelibrary.wiley.com/doi/10.1002/cne.902920402

[11] K. Rohrschneider, "Determination of the Location of the Fovea on the Fundus," *Investigative Opthalmology & Visual Science*, vol. 45, no. 9, p. 3257, Sep. 2004. [Online]. Available: http://iovs.arvojournals.org/article.aspx?doi=10.1167/iovs.03-1157

[12] H. A. Quigley, "The Size and Shape of the Optic Disc in Normal Human Eyes," *Archives of Ophthalmology*, vol. 108, no. 1, p. 51, Jan. 1990. [Online]. Available: http://archopht.jamanetwork.com/article.aspx?doi=10.1001/archopht.1990.01070030057028

[13] "Calculation of Visual Angle." [Online]. Available: https://www.yorku.ca/eye/visangle.htm

[14] Il Yong Yoon, Jong-Mo Seo, Hyoungwon Baac, Byoungho Lee, Sung June Kim, Hyeoung Gon Yu, Young Suk Yu, and Hum Chung, "A new image signal transfer method using laser in artificial retina," in

*First International IEEE EMBS Conference on Neural Engineering, 2003. Conference Proceedings.* Capri Island, Italy: IEEE, 2003, pp. 208–210. [Online]. Available: http://ieeexplore.ieee.org/document/1196794/

[15] F. Rieke and D. A. Baylor, "Single-photon detection by rod cells of the retina," *Reviews of Modern Physics*, vol. 70, no. 3, pp. 1027–1036, Jul. 1998. [Online]. Available: https://link.aps.org/doi/10.1103/RevModPhys.70.1027

[16] J. Reingruber, D. Holcman, and G. L. Fain, "How rods respond to single photons: Key adaptations of a G-protein cascade that enable vision at the physical limit of perception," *BioEssays*, vol. 37, no. 11, pp. 1243–1252, Nov. 2015. [Online]. Available: https://onlinelibrary.wiley.com/doi/10.1002/bies.201500081

[17] H. Okawa and A. P. Sampath, "Optimization of Single-Photon Response Transmission at the Rod-to-Rod Bipolar Synapse," *Physiology*, vol. 22, no. 4, pp. 279–286, Aug. 2007. [Online]. Available: https://www.physiology.org/doi/10.1152/physiol.00007.2007

[18] G. D. Field, A. P. Sampath, and F. Rieke, "RETINAL PROCESSING NEAR ABSOLUTE THRESHOLD: From Behavior to Mechanism," *Annual Review of Physiology*, vol. 67, no. 1, pp. 491–514, Mar. 2005. [Online]. Available: https://www.annualreviews.org/doi/10.1146/annurev.physiol.67.031103.151256

[19] P. Sterling, M. Freed, and R. Smith, "Architecture of rod and cone circuits to the on-beta ganglion cell," *The Journal of Neuroscience*, vol. 8, no. 2, pp. 623–642, Feb. 1988. [Online]. Available: https://www.jneurosci.org/lookup/doi/10.1523/JNEUROSCI.08-02-00623.1988

[20] D. Takeshita, L. Smeds, and P. Ala-Laurila, "Processing of single-photon responses in the mammalian On and Off retinal pathways at the sensitivity limit of vision," *Philosophical Transactions of the Royal Society B: Biological Sciences*, vol. 372, no. 1717, p. 20160073, Apr. 2017. [Online]. Available: https://royalsocietypublishing.org/doi/10.1098/rstb.2016.0073

[21] P. Ala-Laurila and F. Rieke, "Coincidence Detection of Single-Photon Responses in the Inner Retina at the Sensitivity Limit of Vision," *Current Biology*, vol. 24, no. 24, pp. 2888–2898, Dec. 2014. [Online]. Available: https://linkinghub.elsevier.com/retrieve/pii/S0960982214013372

[22] D. A. Baylor, G. Matthews, and K. W. Yau, "Two components of electrical dark noise in toad retinal rod outer segments." *The Journal of Physiology*, vol. 309, no. 1, pp. 591–621, Dec. 1980. [Online]. Available: https://onlinelibrary.wiley.com/doi/10.1113/jphysiol.1980.sp013529

[23] J. Pahlberg and A. P. Sampath, "Visual threshold is set by linear and nonlinear mechanisms in the retina that mitigate noise: How neural circuits in the retina improve the signal-to-noise ratio of the single-photon response," *BioEssays*, vol. 33, no. 6, pp. 438–447, Jun. 2011. [Online]. Available: https://onlinelibrary.wiley.com/doi/10.1002/bies.201100014

[24] D. A. Baylor, B. J. Nunn, and J. L. Schnapf, "The photocurrent, noise and spectral sensitivity of rods of the monkey Macaca fascicularis." *The Journal of Physiology*, vol. 357, no. 1, pp. 575–607, Dec. 1984. [Online]. Available: https://onlinelibrary.wiley.com/doi/10.1113/jphysiol.1984.sp015518

[25] G. D. Field, V. Uzzell, E. J. Chichilnisky, and F. Rieke, "Temporal resolution of single-photon responses in primate rod photoreceptors and limits imposed by cellular noise," *Journal of Neurophysiology*, vol. 121, no. 1, pp. 255–268, Jan. 2019. [Online]. Available: https://www.physiology.org/doi/10.1152/jn.00683.2018

[26] J. Reingruber, J. Pahlberg, M. L. Woodruff, A. P. Sampath, G. L. Fain, and D. Holcman, "Detection of single photons by toad and mouse rods," *Proceedings of the National Academy of Sciences*, vol. 110, no. 48, pp. 19 378–19 383, Nov. 2013. [Online]. Available: https://pnas.org/doi/full/10.1073/pnas.1314030110

[27] M. Van Rossum and R. Smith, "Noise removal at the rod synapse of mammalian retina," *Visual Neuroscience*, vol. 15, no. 5, pp. 809–821, May 1998. [Online]. Available: https://www.cambridge.org/core/product/identifier/S0952523898155037/type/journal_article

[28] G. D. Field and F. Rieke, "Nonlinear Signal Transfer from Mouse Rods to Bipolar Cells and Implications for Visual Sensitivity," *Neuron*, vol. 34, no. 5, pp. 773–785, May 2002. [Online]. Available: https://linkinghub.elsevier.com/retrieve/pii/S0896627302007006

[29] H. Snijders, J. Frey, J. Norman, V. Post, A. Gossard, J. Bowers, M. Van Exter, W. Löffler, and D. Bouwmeester, "Fiber-Coupled

Cavity-QED Source of Identical Single Photons," *Physical Review Applied*, vol. 9, no. 3, p. 031002, Mar. 2018. [Online]. Available: https://link.aps.org/doi/10.1103/PhysRevApplied.9.031002

[30] P. Steindl, H. Snijders, G. Westra, E. Hissink, K. Iakovlev, S. Polla, J. Frey, J. Norman, A. Gossard, J. Bowers, D. Bouwmeester, and W. Löffler, "Artificial Coherent States of Light by Multiphoton Interference in a Single-Photon Stream," *Physical Review Letters*, vol. 126, no. 14, p. 143601, Apr. 2021. [Online]. Available: https://link.aps.org/doi/10.1103/PhysRevLett.126.143601

[31] R. Holmes, M. Victora, R. F. Wang, and P. G. Kwiat, "Measuring temporal summation in visual detection with a single-photon source," *Vision Research*, vol. 140, pp. 33–43, Nov. 2017. [Online]. Available: https://linkinghub.elsevier.com/retrieve/pii/S0042698917301438

[32] M. Fox, *Quantum optics: an introduction*, ser. Oxford master series in physics. Oxford ; New York: Oxford University Press, 2006, no. 15.

[33] "Essential laser beam parameters to know about your laser system," Dec. 2023. [Online]. Available: https://www.gentec-eo.com/blog/laser-beam-parameters

[34] D. R. Paschotta, "Gaussian beams." [Online]. Available: https://www.rp-photonics.com/gaussian_beams.html

[35] E. Galvez, *Gaussian Beams*. Colgate University, 2014.

[36] "When to Use the D86 Beam Width Measurement Method." [Online]. Available: https://dataray.com/blogs/dataray-blog/when-to-use-the-d86-beam-width-measurement-method

[37] "Scale Model of Human Eye." [Online]. Available: http://hyperphysics.phy-astr.gsu.edu/hbase/vision/eyescal.html

[38] "Single Mode FC/PC Fiber Optic Patch Cables." [Online]. Available: https://www.thorlabs.com/newgrouppage9.cfm?objectgroup_id=1362

[39] J. B. Jonas, U. Schneider, and G. O. H. Naumann, "Count and density of human retinal photoreceptors," *Graefe's Archive for Clinical and Experimental Ophthalmology*, vol. 230, no. 6, pp. 505–510, Oct. 1992. [Online]. Available: http://link.springer.com/10.1007/BF00181769

[40] R. Kingslake and R. R. Shannon, Eds., *Applied optics and optical engineering. Vol. 11*. New York: Acad. Press, 1992, vol. 11.

[41] "Spherical Aberration." [Online]. Available: http://hyperphysics.phy-astr.gsu.edu/hbase/geoopt/aber.html#c1

[42] T. J. Lambert and J. C. Waters, "Navigating challenges in the application of superresolution microscopy," *Journal of Cell Biology*, vol. 216, no. 1, pp. 53–63, Jan. 2017. [Online]. Available: https://rupress.org/jcb/article/216/1/53/46128/Navigating-challenges-in-the-application-of

[43] SPQR, "The human visual system : focus and acuity," May 2022. [Online]. Available: https://pixelcraft.photo.blog/2022/05/16/the-human-visual-system-focus-and-acuity/